



Cite this: *J. Mater. Chem. C*, 2017, 5, 2318

Comparative assessment of the strain-sensing behaviors of polylactic acid nanocomposites: reduced graphene oxide or carbon nanotubes†

Chao Hu,^a Zeyu Li,^a Yalong Wang,^a Jiachen Gao,^a Kun Dai,^{*a} Guoqiang Zheng,^a Chuntai Liu,^a Changyu Shen,^a Haixiang Song^b and Zhanhu Guo^{*b}

Reduced graphene oxide (RGO)/polylactic acid (PLA) and carbon nanotubes (CNTs)/PLA nanocomposites were prepared by ultrasound-assisted dispersion and a hot-pressing method for comparative studies. The RGO and CNT nanofillers, which had a hydrogen-bonding interaction with the PLA matrix, were uniformly dispersed in the PLA matrix, and low percolation thresholds (0.11 wt% for RGO/PLA and 0.80 wt% for the CNTs/PLA nanocomposites) were achieved in the PLA nanocomposites. The addition of RGO resulted in weak crystallization ability and significant enhancement in thermal stability of the PLA matrix owing to the two-dimensional characteristic of RGO, while opposite results were obtained for the CNTs nanocomposites (the degree of crystallinity X_c is 49.82% for 0.8 wt% CNTs and 9.21% for 0.8 wt% RGO, respectively). During ten extension–retraction cycles, the values of the max and min $\Delta R/R_0$ for the RGO/PLA nanocomposites shift upwards gradually with the increase of the cycle number, resulting from the breakdown of conductive networks caused by the slippage of overlapped RGO layers; while the values of the max and min $\Delta R/R_0$ for CNTs/PLA nanocomposites decrease gradually owing to the formation of a better conductive network caused by the rearrangement of CNTs. This study is meaningful for the application of conductive polymer composite based strain sensors in many fields, such as structural health monitoring, wearable electronic devices, soft robotics, etc.

Received 5th December 2016,
Accepted 30th January 2017

DOI: 10.1039/c6tc05261d

rsc.li/materials-c

1. Introduction

Conductive polymer composites (CPCs), which are prepared by incorporating conductive fillers into a polymer matrix, have been investigated widely owing to their sensitivity to external stimuli including thermal field,^{1,2} humidity,^{3,4} chemical vapors,^{5–7} external stress field,^{8–10} etc. In the past few years, the strain-sensing behaviors of CPCs composed of carbon nanotubes (CNTs) and graphene have been investigated more and more extensively for their promising applications in strain sensing devices. For example, Vertuccio *et al.*¹¹ reported the electrical resistance variations of multi-walled carbon nanotubes (MWCNTs)/epoxy (EP) nanocomposites when subjected to differently applied strains. Their study indicated that the gauge factor of CPCs decreased from 4.45 to 0.67 with the increase of the MWCNT content from 0.050 to 0.5 wt%, and a nonlinear behavior was observed when

the MWCNT content was as low as 0.025 wt%. A novel hybrid filler, graphene-functionalized carbon nanotubes (CNTs–graphene), was used to improve the strain sensing properties of a poly(vinylidene fluoride) (PVDF) based composite by Ramaprabhu *et al.*¹² The gauge factor for 3 wt% CNTs–graphene/PVDF composites is about 20, and the value decreases with a further increase in the concentration of the CNTs–graphene nanofiller. Zhang *et al.*¹³ studied the strain-sensing behaviors of MWCNTs/thermoplastic polyurethane (TPU) under dynamic strain. They found that the resistance responses of 0.2 wt% CNTs/TPU composites had good reproducibility and recoverability at a strain of 5%. However, a double peak caused by the competition between network breakdown and reformation during loading and unloading of the composites appears when a large strain was applied (30%).

Due to the outstanding characteristics of graphene, such as a large aspect ratio and high electrical conductivity, the strain-sensing behaviors of CPCs filled with graphene have attracted tremendous attention in recent years. For example, Ramaprabhu *et al.*¹⁴ reported a simple one-step method for the preparation of reduced graphene oxide (RGO)/PVDF composites. For the RGO/PVDF composites around the percolation threshold (2 wt%), the composites show a very high gauge factor (12.1), which is in

^a School of Materials Science and Engineering, The Key Laboratory of Material Processing and Mold of Ministry of Education, Zhengzhou University, Zhengzhou, Henan 450001, P. R. China. E-mail: kundai@zzu.edu.cn

^b Integrated Composites Laboratory (ICL), Department of Chemical & Biomolecular Engineering, University of Tennessee, Knoxville, TN 37996, USA. E-mail: zguo10@utk.edu

† Electronic supplementary information (ESI) available. See DOI: 10.1039/c6tc05261d

conformity with other reports.¹⁵ Chen *et al.*¹⁶ found that the piezoelectric behaviors of graphite nanosheets (GNs)/polyethylene (PE) composites were strongly dependent on the GN concentration and the spatial arrangement of GNs. The conducting network constructed by the orientated GNs would be more sensitive to compression. Liu *et al.*¹⁷ studied the effect of graphene contents, strain amplitudes and strain rates on the strain-sensing behaviors of graphene/TPU nanocomposites. It revealed that graphene/TPU nanocomposites exhibited good sensing stability in diverse strain modes (the gauge factor ranging from 0.78 of 0.6 wt% graphene/TPU at a strain rate of 0.1 min⁻¹ to 17.7 of 0.2 wt% graphene/TPU at a strain rate of 0.3 min⁻¹). A comparative investigation of strain-sensing behaviors of CPCs filled by different dimensional nanofillers has also been reported. For example, Deng *et al.*⁸ investigated the strain-sensing behaviors of CPCs by the use of hybrid carbon fillers and functionalized CNTs. They found that the conductive network formed by hybrid fillers of MWCNTs and carbon black exhibited higher resistance sensitivity to strain. The combination of mixed fillers and functionalized CNTs could enhance the resistance sensitivity further based on the improved interfacial interaction between nanofillers and the polymer matrix (the gauge factor ranging from 5 to 140 238). Zhao *et al.*¹⁸ compared the strain-sensing behaviors of carbon black/polypropylene (PP) and CNTs/PP CPCs. The dimension and interaction of conductive fillers played a pivotal role in the evolution of the conductive network in tension. Although many research studies have investigated the morphology, electronic, thermal and mechanical properties of the RGO/poly(lactic acid) (PLA) composites,^{19–22} the strain sensing behaviors of the RGO/PLA composites have rarely been studied so far. In particular, as one of the most important biocompatible and biodegradable materials,^{23,24} PLA incorporated with conductive fillers for strain sensors would promise multipurpose potential applications in the fields of bio-nanomaterials and eco-friendly functional materials.

The physical properties of the polymer, dispersion and aspect ratio of conductive fillers play a crucial role in the evolution of conducting networks when the CPCs are under tension. Several research studies have been conducted on strain sensors based on MWCNTs or graphene for electronic applications in wearable strain sensors, robotics, artificial skin and healthcare,^{25–27} depending on the type of materials (*e.g.*, silicone-based elastomers and thermoplastic elastomers^{28–30}), microstructures (*e.g.*, microcracks, microchannels and micropores^{31–33}), fabrication processes (*e.g.*, electrospinning, spin-coating and chemical vapor deposition^{34,35}), *etc.* Although the strain-sensing behaviors of CPCs blended with CNTs or RGO have been investigated by a number of researchers in recent years, the influence of dimension and interconnection of the two conductive fillers on the evolution of conductive networks of CPCs under strain has rarely been investigated.

Herein, CNTs and RGO were selected as one- and two-dimensional conductive fillers and PLA as the matrix to prepare their nanocomposites. The morphology and microstructure of conductive fillers and the nanocomposites were studied firstly.

The influence of the filler morphology on the crystallization, melting behaviors and thermal stability of the PLA nanocomposites was discussed. Finally, the strain-sensing behaviors of both CPCs were studied and compared.

2. Experimental

2.1. Materials and chemicals

PLA (4032D), supplied by NatureWorks, has M_w and M_n of about 2.23×10^5 and 1.06×10^5 g mol⁻¹, respectively. PLA was dried in a vacuum oven at 80 °C for 10 h before usage to get rid of water. MWCNTs and RGO were both supplied by Chengdu Organic Chemicals, Chinese Academy of Science. The diameter of MWCNTs was in the range of 10–40 nm and the length was about 50 μm. The size of RGO was about 0.5–3 μm and the thickness was about 0.55–3.74 nm. Dimethylformamide (DMF) and ethanol were purchased from Zhiyuan Reagent Co., Ltd, Tianjin, China, and used as received.

2.2. Fabrication of PLA based CPCs

The PLA based CPCs were prepared by using solution blending followed by hot compression molding (Fig. 1). Briefly, the desired amount of conductive nanofillers was initially dispersed in 100 mL DMF with the assistance of sonication at room temperature for 10 min. Then 5 g of PLA was added into the obtained suspension. After agitation at 80 °C for 50 min using a magnetic stirrer and sonication in the room temperature water bath for another 30 min, the mixture was coagulated with ethanol (800 mL). The flocculate was filtered under vacuum, and then vacuum dried at 80 °C for 12 h. The neat PLA sample was fabricated in the same manner for the sake of comparison. The obtained material was then compression molded into 0.45 mm thick sheets at 185 °C under a pressure of 5 MPa. The specimens for tests were prepared by cutting these sheets into strips with dimensions of 30 mm (length) × 10 mm (width). In the present paper, different nanocomposites are denoted as “x-CNTs/PLA” and “x-RGO/PLA” for simplicity, where x denotes the weight percentages of CNTs and RGO.

2.3. Characterization

The morphology of RGO and RGO/PLA CPC was investigated by transmission electron microscopy (TEM, JEOL JEM-1230) at an acceleration voltage of 90 kV. The morphology of CNTs was investigated using a field emission scanning electron microscope (FE-SEM, JEOL JSM-7500F). X-ray diffraction (XRD) patterns of PLA and its CPCs were recorded at room temperature in the reflection mode using a Rigaku Ultima IV diffractometer. Fourier transform infrared (FTIR) measurements were performed on a Thermo Fisher Nicolet iS50 spectrometer in the attenuated total reflection (ATR) mode.

A ZC-36 high-resistance meter (Shanghai Cany Precision Instruments Co., Ltd) was used to measure conductivity lower than 10⁻⁶ S m⁻¹, and the samples with volume electrical conductivities higher than 10⁻⁶ S m⁻¹ were measured using a Tektronix Digital Multimeter (model DMM4050). The volume

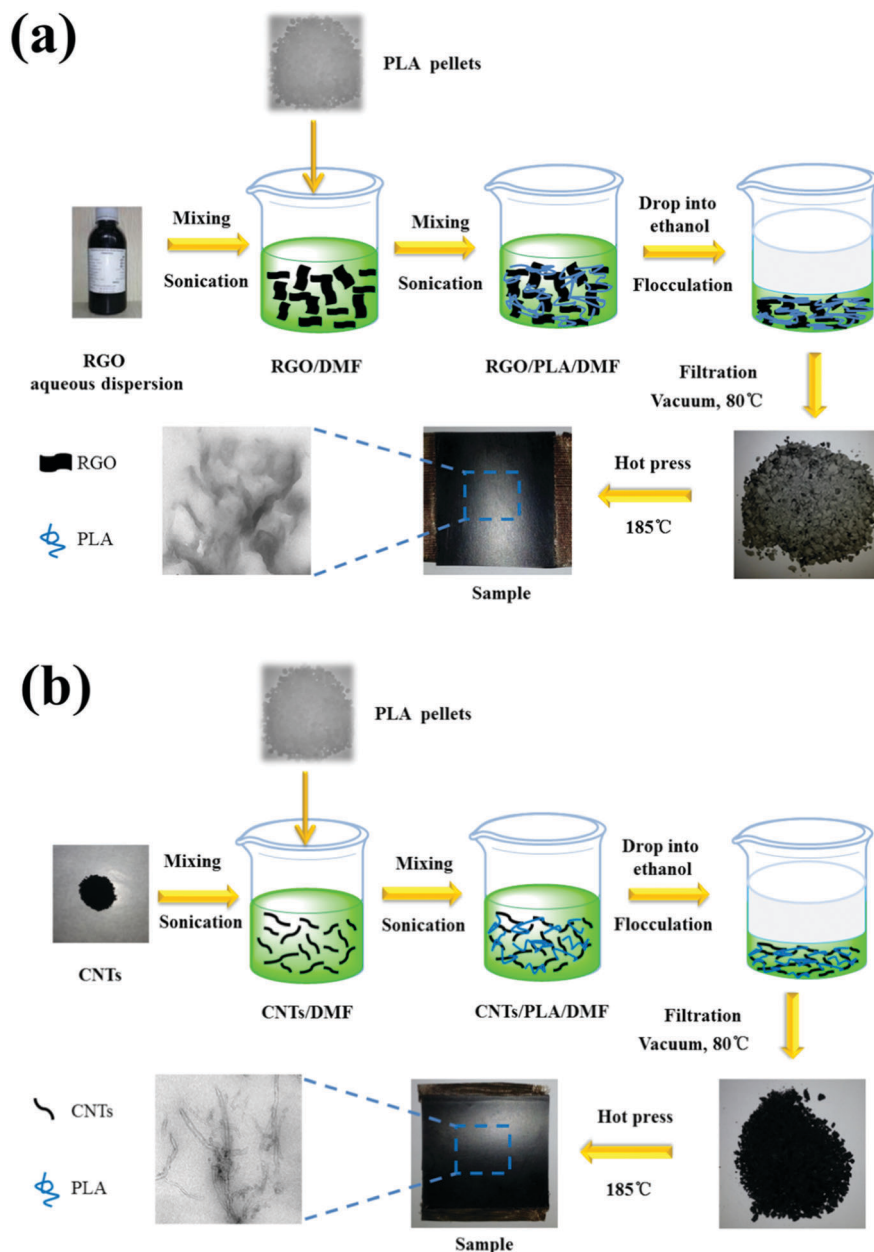


Fig. 1 Schemes of the process for the fabrication of PLA nanocomposites by co-coagulation plus compression molding technique: (a) RGO/PLA nanocomposites and (b) CNTs/PLA nanocomposites.

electrical conductivity σ was calculated using the equation $\sigma = 1/\rho = L/RS$, where ρ is the electrical resistivity, L is the length between the electrodes, R is the volume resistance, and S is the cross-sectional area of the specimen.

Thermal analysis of neat PLA and its nanocomposites was performed under nitrogen flow using a differential scanning calorimeter (DSC, TA Instruments Q 2000). The samples were heated from 40 to 200 °C at a rate of 20 °C min⁻¹, and then cooled to 20 °C at the same rate. In order to investigate the nucleation effect distinction of the two nanofillers clearly, the samples were then heated to 200 °C at a rate of 5 °C min⁻¹.³⁶ Cold-crystallization peak temperature (T_{cc}), melt temperature (T_m), cold crystallization enthalpy (ΔH_{cc}) and melting enthalpy (ΔH_m) were determined from the second heating

scans by using the instrument software. Subsequently, the samples were cooled to 20 °C at a rate of 5 °C min⁻¹. The crystallinity (X_c) of PLA and its nanocomposites was calculated using eqn (1).³⁷

$$X_c = \frac{\Delta H}{\Delta H_m^0 \cdot (1 - x)} \times 100\% \quad (1)$$

where $\Delta H = \Delta H_m - \Delta H_{cc}$. ΔH_m^0 is the melting enthalpy of the 100% crystalline PLA matrix (93.6 J g⁻¹ for PLA³⁸) and x is the weight percentage of RGO or CNT nanofillers.

Thermogravimetric analysis (TGA) was carried out using TGA (TA Instruments, Q50) from 30 to 700 °C under a nitrogen atmosphere at 10 °C min⁻¹. The thermal degradation temperatures were defined as the temperature with a weight loss of 5% (T_{d5}) and the temperatures

corresponding to the maximum DTG peaks (T_{\max}) were obtained from the first derivative curve of the TGA thermograph.

For the strain sensing test, the electrical resistance upon cyclic loading was recorded using a self-made online recording device (Fig. S1, ESI[†]) as in our previous work.^{17,18} The original resistances of both CPCs for experiments were all about $6 \times 10^{-4} \text{ S m}^{-1}$. Ten extension–retraction cycles were conducted at the loading and unloading speed of 0.5 mm min^{-1} to study the strain-sensing behaviors of CPCs. The gauge length in the test was 30 mm. Two copper electrodes separated by 10 mm were bonded with silver paste to achieve good contact between electrodes and the samples (Fig. S2, ESI[†]).

3. Results and discussion

3.1. Morphology and microstructure of conductive nanofillers and PLA based CPCs

In order to study the effect of conductive nanofillers on the thermal, mechanical and electrical properties, it is essential to

study the morphology of CNTs, RGO and its dispersion state in the polymer matrix. Fig. 2(a and b) show the typical morphology of RGO and CNT nanoparticles used in this paper. As shown in Fig. 2(a), the surface of RGO shows a two-dimensional layered structure and looks like a piece of crumpled, wrinkled and folded thin paper. These characteristics make RGO more effective in constructing a conductive network through plane-to-plane contact. In Fig. 2(b), we can observe that CNTs, which exhibit a one-dimensional tube characteristic, entangle with each other. These characteristics make the CNTs beneficial to construct a stable conductive network in the polymer matrix. The dispersion state of CNTs and RGO in the PLA matrix containing 1 wt% RGO and 1 wt% CNTs was studied by TEM, respectively. As shown in Fig. 2(c and d), the CNTs and RGO nanofillers are observed to be distributed uniformly throughout the PLA matrix with no obvious aggregation.

Fig. 2(e) shows the XRD patterns of neat PLA and its nanocomposites with different concentrations of CNTs and RGO. The XRD patterns of PLA and its nanocomposites are manifested by

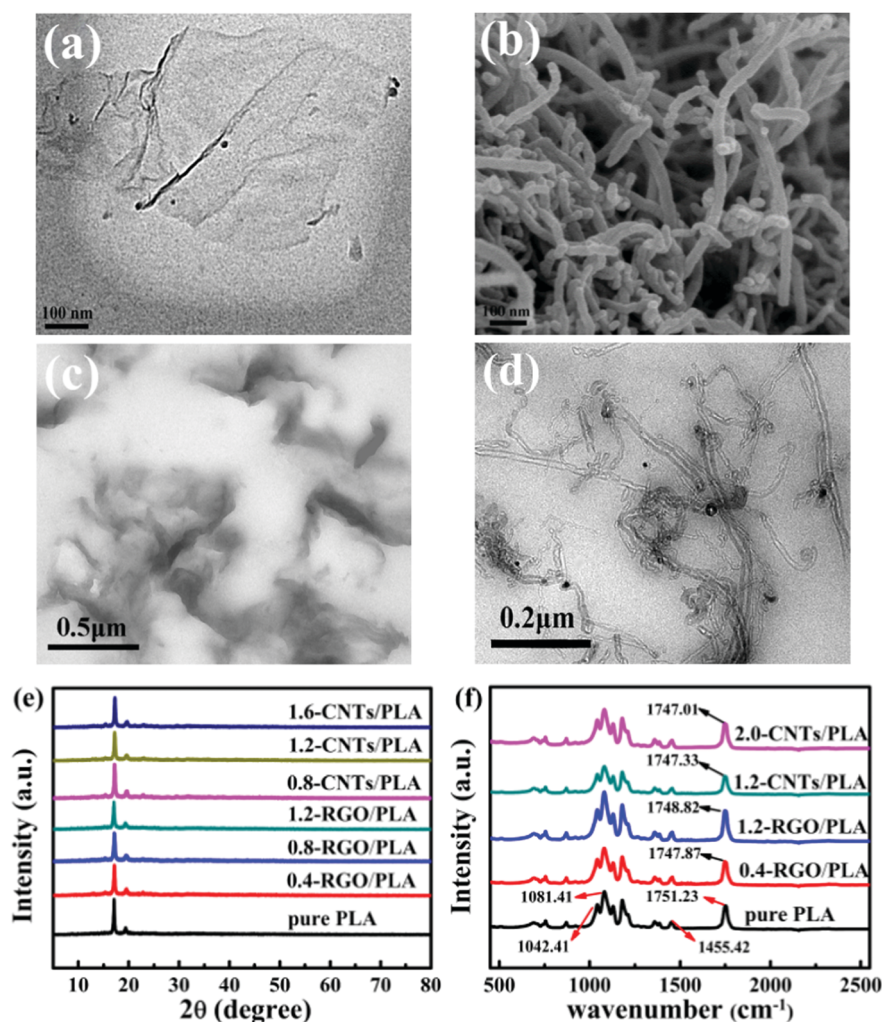


Fig. 2 (a) TEM images of RGO at a high magnification; (b) SEM images of CNTs at a high magnification; TEM micrographs of PLA based CPCs: (c) RGO/PLA (1 wt%) and (d) CNTs/PLA (1 wt%); (e) XRD patterns of neat PLA and its nanocomposites with different RGO or CNT concentrations; (f) FTIR spectra of neat PLA and its nanocomposites with different RGO or CNT concentrations.

the characteristic diffraction peaks around 16.7° and 19.0° , which are assigned to (200)/(110) and (203) planes of crystalline PLA, respectively. Additionally, it is generally believed that XRD patterns of the restacked RGO layers would exhibit a broad diffraction peak at 26° .³⁹ However, the XRD patterns of RGO/PLA nanocomposites with different RGO loadings do not present the diffraction peak at 26° , implying that the RGO does not reaggregate obviously during the composite processing.⁴⁰

The interaction between the nanofillers and the PLA matrix was investigated by FTIR. As shown in Fig. 2(f), the absorption peak of pure PLA at 1455.42 cm^{-1} is assigned to the asymmetric bending of $-\text{CH}_3$. The bands at 1081.41 and 1042.41 cm^{-1} represent the C–O stretching vibration. The carbonyl (C=O) stretching band of pure PLA is reflected at 1751.23 cm^{-1} . When 0.4 wt% RGO or 1.2 wt% CNTs was added to PLA, the C=O peak of PLA shifted from 1751.23 to 1747.87 or 1747.33 cm^{-1} , respectively. This phenomenon can be attributed to the hydrogen bonding interaction between the groups of RGO or CNTs and the C=O group of PLA chains. Similar interaction has also been reported in RGO/polyurethane systems.⁴¹

3.2. Crystallization and melting behaviors of PLA and its nanocomposites

A comparison between the thermal properties of CNTs and RGO nanocomposites was done by DSC. Fig. 3(a and b) show the DSC curves of PLA and its nanocomposites. As shown in Fig. 3(a), all specimens are characterized by a distinct cold crystallization peak. The cold-crystallization peak temperature (T_{cc}) of RGO/PLA nanocomposites shifts downward compared to that of neat PLA.

(The T_{cc} shifts from 104.81°C for pure PLA to 94.05°C for 0.2-RGO/PLA nanocomposites.) The decrease of T_{cc} is attributed to the nucleating effect of RGO, which promotes the crystallization kinetics of PLA. However, with further increasing the RGO concentration, the interaction between RGO and PLA phases restricts the motion of PLA chains,¹⁹ resulting in an obviously increased T_{cc} in the RGO/PLA nanocomposites (the T_{cc} increases from 90.45°C for 0.2-RGO/PLA to 108.01°C for 1.2-RGO/PLA). These phenomena correspond to the results of the cooling cycle. As shown in Fig. 3(c), the DSC curve of neat PLA in the cooling process shows no obvious crystallization peak, which is confirmed by the shortage of the crystallization peak. It deserves to be emphasized that the addition of 0.2 wt% RGO in PLA induces the PLA crystallization in the cooling process. However, when the concentration of RGO is further increased to 1.2 wt%, the crystallization peaks of RGO/PLA nanocomposites disappear again during cooling. The main reason is that the RGO nanoparticles can act as nucleation agents for the crystallization of PLA, resulting in an apparent crystallization peak. On the other hand, with the further increase of RGO concentration, the presence of excessive RGO will restrict the polymer chain movement and hinder the crystal growth, resulting in the fading of the crystallization peak. In particular, the T_m of the RGO/PLA nanocomposites is similar to each other with different RGO concentrations.

As shown in Fig. 3(b), the cold crystallization peak of all specimens containing CNTs disappear during heating. While the crystallization peaks of CNTs/PLA nanocomposites are observed obviously during cooling, Fig. 3(d). Meanwhile, the presence of

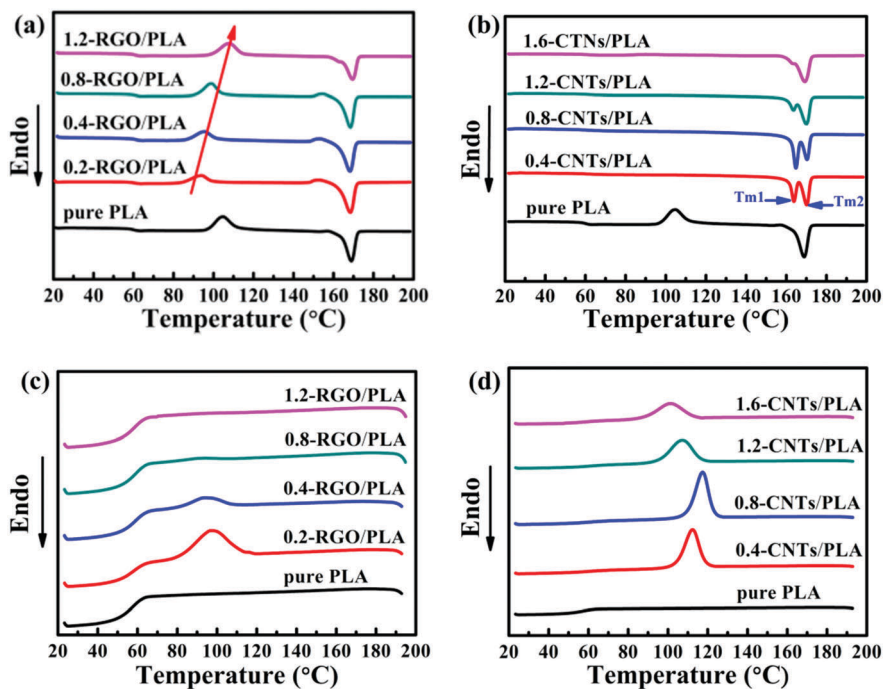


Fig. 3 DSC curves of PLA and its nanocomposites during heating: (a) PLA and RGO/PLA nanocomposites and (b) PLA and CNTs/PLA nanocomposites. DSC curves of PLA and its nanocomposites during cooling: (c) PLA and RGO/PLA nanocomposites and (d) PLA and CNTs/PLA nanocomposites. The heating and cooling rates are both 5°C min^{-1} .

Table 1 Detailed information derived from the second heating DSC scan for neat PLA and its nanocomposites

Sample	T_{cc} (°C)	T_m (°C)	ΔH_{cc} (J g ⁻¹)	ΔH_m (J g ⁻¹)	X_c (%)
PLA	104.81	168.94	36.67	45.55	9.49
0.2-RGO/PLA	94.05	168.42	23.45	41.25	19.06
0.4-RGO/PLA	95.65	168.27	27.35	38.97	12.46
0.8-RGO/PLA	99.02	168.44	31.31	39.86	9.21
1.2-RGO/PLA	108.01	169.53	33.05	40.03	7.55
0.4-CNTs/PLA	—	170.18	—	49.87	53.49
0.8-CNTs/PLA	—	170.55	—	46.26	49.82
1.2-CNTs/PLA	—	169.45	—	45.68	49.40
1.6-CNTs/PLA	—	169.03	—	41.55	45.11

The T_m of CNTs/PLA nanocomposites is defined as the peak temperature of the main endotherm in multiple endothermic peaks.

CNTs shifts the melt crystallization temperature (T_{mc}) of CNTs/PLA nanocomposites to higher temperature and then to lower temperature with the increase of CNT concentration. These results suggest that CNTs not only act as nucleation agents to promote the crystallization of PLA but also restrict the segmental motions of PLA to some extent, especially at a higher CNT content. Interestingly, compared with Fig. 3(a), DSC heating curves of CNTs/PLA nanocomposites in Fig. 3(b) show two melting peaks at T_{m1} and T_{m2} , which are related to the thin lamellae and the thickened crystals of PLA, respectively.⁴²

Table 1 shows that the presence of RGO in the PLA phase does not affect the crystallization of PLA noticeably, but affect the T_{cc} distinctly. Contrarily, the presence of CNTs in the PLA phase leads to a considerable increase of crystallinity and the vanishing of cold crystallization behavior as well compared to pure PLA (X_c is 9.49%). The X_c of RGO/PLA nanocomposites

decreased from 19.06% for 0.2-RGO/PLA to 7.55% for 1.2-RGO/PLA. Whereas the addition of 0.4% and 1.6% CNTs leads to considerably higher crystallinity (X_c is 53.49% for 0.4% CNTs and 45.11% for 1.6% CNTs, respectively). These results suggest that the ability of CNTs to induce the crystallization behavior of PLA is stronger than that of RGO.

3.3. Thermogravimetric analysis (TGA)

In order to investigate the effect of the dimension of the nanofillers on the thermal stability of the PLA matrix, TGA analysis was carried out for PLA and its nanocomposites under a nitrogen atmosphere at a heating rate of 10 °C min⁻¹. As shown in Fig. 4(a) and Table 2, the T_{d5} for neat PLA and 0.4-RGO/PLA nanocomposites is 322.68 and 334.77 °C, respectively. The enhancement of T_{d5} for the RGO/PLA nanocomposites could be explained by the mass barrier effects of RGO, which retards the organic combustion and acts as a gas barrier for preventing the emission of the produced degradation gases.⁴³ Contrarily, the thermal stability of the PLA matrix is reduced by the addition of CNTs. As shown in Fig. 4(b) and Table 3, the T_{d5} of CNTs/PLA nanocomposites decreased evidently with an increase in the concentration of CNTs. The T_{d5} for neat PLA and 1.6-CNTs/PLA nanocomposites is 322.68 and 312.94 °C, respectively. Such a decrease could be attributed to the high heat conductivity of CNTs, which makes heat diffuse easier and faster in the PLA matrix. These phenomena indicate that the CNTs with a one-dimensional tube microstructure exhibit good heat conductivity but a poor mass barrier effect. As shown in Tables 2 and 3, compared with neat PLA, the T_{max} of RGO/PLA nanocomposites has slightly increased. However, the T_{max} of CNTs/PLA nanocomposites remains virtually unchanged.

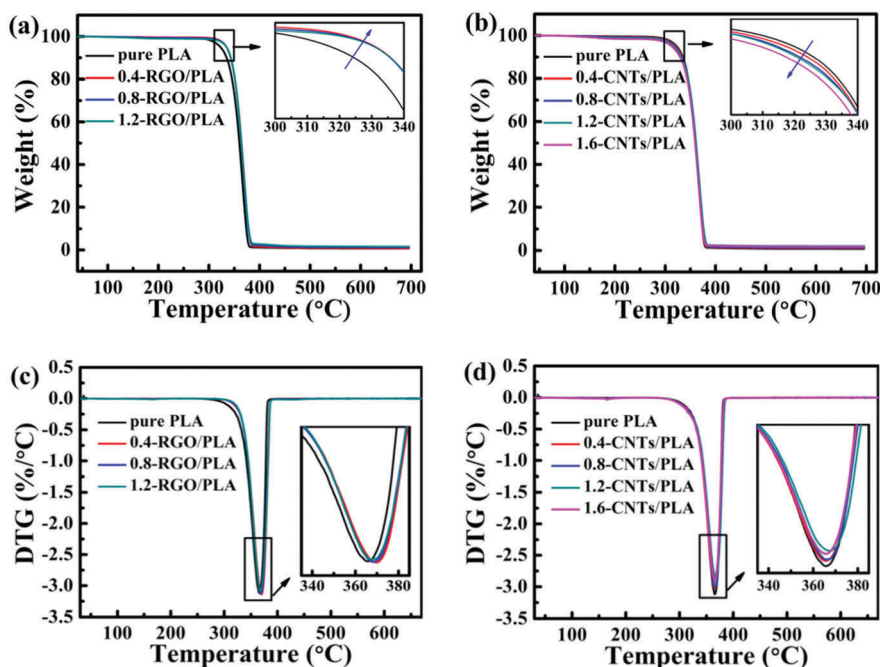


Fig. 4 TGA curves of PLA and its nanocomposites under nitrogen: (a) PLA and RGO/PLA nanocomposites and (b) PLA and CNTs/PLA nanocomposites; DTG curves of PLA and its nanocomposites: (c) PLA and RGO/PLA nanocomposites and (d) PLA and CNTs/PLA nanocomposites. The insets in (a)–(d) show the corresponding magnified curves encompassed by the boxes in the main images.

Table 2 TGA and DTA results of PLA and RGO/PLA nanocomposites

Sample	T_{ds} ($^{\circ}\text{C}$)	T_{max} ($^{\circ}\text{C}$)
PLA	322.68	365.88
0.4-RGO/PLA	334.77	369.73
0.8-RGO/PLA	334.46	368.17
1.2-RGO/PLA	334.59	367.81

Table 3 TGA and DTA results of PLA and CNTs/PLA nanocomposites

Sample	T_{ds} ($^{\circ}\text{C}$)	T_{max} ($^{\circ}\text{C}$)
PLA	322.68	365.88
0.4-CNTs/PLA	320.39	365.60
0.8-CNTs/PLA	317.75	366.11
1.2-CNTs/PLA	316.72	367.33
1.6-CNTs/PLA	312.94	365.64

3.4. Electrical conductivity of PLA nanocomposites

Before the strain-sensing behavior test, the percolation behaviors of both CPCs were studied and compared firstly. Fig. 5 shows the volume conductivity *versus* the mass fraction of CNTs and RGO nanofillers in CNTs/PLA and RGO/PLA nanocomposites. For RGO/PLA nanocomposites, the electrical conductivity shows a rapid increase from 2.15×10^{-15} to $3.55 \times 10^{-5} \text{ S m}^{-1}$ with the increase of RGO concentration from 0.1 to 0.6 wt%, which jumps nearly 10 orders of magnitude. The percolation threshold is estimated to be *ca.* 0.11 wt% using the power law function, eqn (2):⁴⁴

$$\sigma(p) = B(p - p_c)^t \quad (2)$$

where $\sigma(p)$ is the experimental conductivity value for the filler content $p > p_c$, B is the conductivity of the nanofillers, p_c is the percolation threshold of the system, and t is the critical exponent.

For CNTs/PLA nanocomposites, the electrical conductivity increases sharply by about 11 orders of magnitude, from 2.74×10^{-15} to $2.36 \times 10^{-4} \text{ S m}^{-1}$, when the concentration of CNTs increases from 0.4 to 1.2 wt%. The percolation threshold is

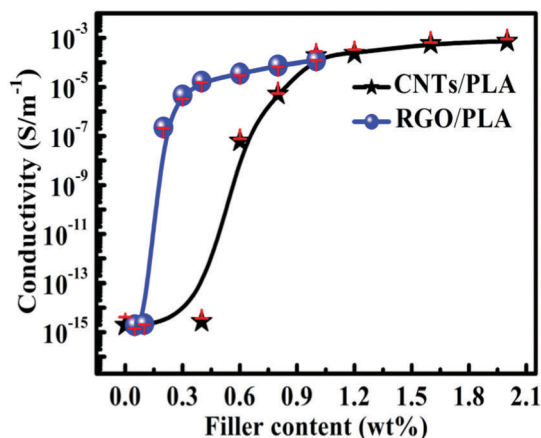


Fig. 5 Volume conductivity vs. CNT and RGO content of CNTs/PLA and RGO/PLA.

estimated to be *ca.* 0.80 wt%, which is higher than the CNTs/PLA. As demonstrated by Yu,⁴⁵ two-dimensional RGO nanosheets with a higher specific surface area can form a conductive network more effectively than one-dimensional CNTs, leading to a lower percolation threshold.

3.5. Mechanical properties of PLA nanocomposites

Fig. 6 shows the mechanical properties of PLA and its nanocomposites filled with 0.5 wt% RGO and 1 wt% CNTs (the room temperature resistivities of the two samples are similar for the strain sensing test, about $6 \times 10^{-4} \text{ S m}^{-1}$ in the present work). The strength and elongation at the break of RGO/PLA and CNTs/PLA nanocomposites changed slightly as compared with pure PLA. These phenomena are related to good dispersion of conductive nanofillers in the PLA matrix and fine interaction between conductive nanofillers and the PLA matrix.^{46,47}

As discussed above, the dimension of the nanofillers has a significant influence on the thermal and electrical properties of PLA based CPCs. It is reported that the resistance of CPCs close to the percolation threshold is remarkably sensitive to tensile strain. Therefore, the CPCs filled with 0.5 wt% RGO and 1 wt% CNTs (the room temperature conductivities of the two samples are similar), which are just beyond the percolation threshold, were also chosen to investigate the strain-sensing behaviors of RGO/PLA and CNTs/PLA nanocomposites. Although the CPCs incorporated with RGO and CNTs were fabricated by the same process, the conductive network microstructures of the CPCs formed by the two-dimensional RGO nanofillers or the one-dimensional CNT nanofillers are undoubtedly different. In order to study the influence of the dimension of the nanofillers on the microstructural evolution of conductive networks under tension, ten extension–retraction cycles of both CPCs were investigated with the maximum strain of 3%.

Ten stress–strain curves of these two CPCs are shown in Fig. 7(a and b). For both CPCs, in each cycle, the stress increases almost linearly with increasing tensile strain until it reaches the maximum strain (the inset in Fig. 7a and b). After the maximum strain, the machine cross-head moved back to strain $\varepsilon = 0$ at the same rate. For both CPCs, due to the hysteresis effect caused by the viscoelastic behavior of the polymer matrix as previously reported in the literature for multi-walled CNTs/vinyl ester composites,⁴⁸ the stress decreases slightly when the strain restores to zero and the maximum stress of both CPCs decreases slightly as well with the increase of the cycle number.

3.6. Mechanical–electrical properties under cyclic tension

In order to study the evolution of conductive networks with the applied tensile load, the stress and $\Delta R/R_0$ (R_0 is the original resistance and ΔR is the instantaneous change in resistance) as a function of the strain in the first tensile cycle for both CPCs were studied (Fig. 8a and b). It is known that the breakdown of the existing conductive networks and reconstruction of new conductive networks occur simultaneously during the tensile process. The $\Delta R/R_0$ of CNTs/PLA nanocomposites displayed a stepwise increase in comparison with that of the RGO/PLA

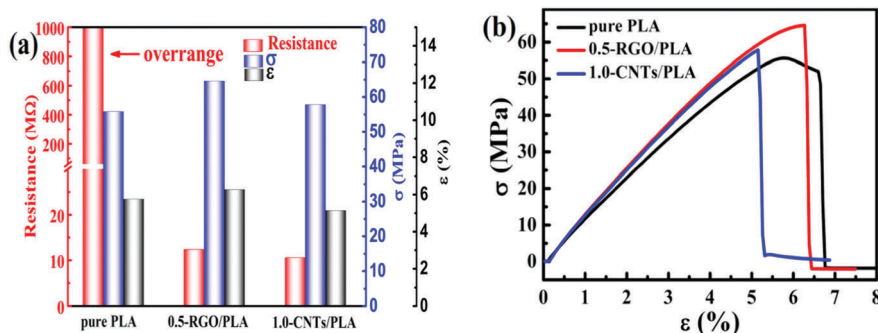


Fig. 6 (a) Mechanical properties of PLA and its nanocomposites; (b) stress–strain curves of PLA and its nanocomposites.

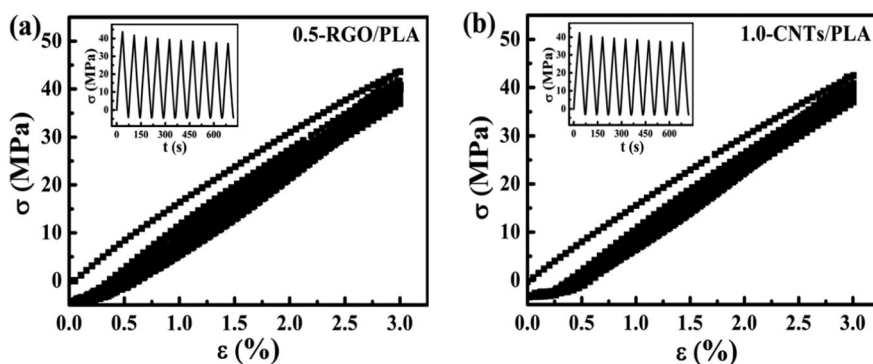


Fig. 7 Relationships of stress vs. strain in (a) 0.5-RGO/PLA and (b) 1.0-CNTs/PLA nanocomposites during 10 extension–retraction cycles, the insets show the plot of stress vs. time (t).

nanocomposites. This phenomenon indicated that, compared to a two-dimensional layered structure of RGO, which constructs a conductive network through plane-to-plane contact,⁴⁹ one-dimensional long tube and entanglement structures of CNTs can balance the reconstruction and breakdown of conductive networks more effectively.

As shown in Fig. 8(c and d), the increase of $\Delta R/R_0$ is observed when both CPCs are subjected to applied strain and $\Delta R/R_0$ decreases with the retraction of strain in each extension–retraction cycle. This can be explained by the fact that the distances between the neighboring conductive nanofillers increase during the extension cycles and decrease during the retraction cycles, leading to an increase of tunneling resistance between adjacent conductive nanofillers during the extension process and a decrease during the retraction process.

However, it is noteworthy that, for RGO/PLA nanocomposites, the values of the max and min $\Delta R/R_0$ shift upwards gradually with the increase of the cycle number (Fig. 8c and e). The mechanism is discussed as follows. The RGO nanosheets can either directly contact each other or be sufficiently neighboring with each other to construct conductive paths through the tunneling effect. In the extension cycle process, the motions of RGO along with PLA macromolecules (the stress transfer taking place from the PLA matrix to RGO⁵⁰) result in the loss of contacts between adjacent RGO particles and the increase of the distance of adjacent RGO, hence leading to the breakdown of conductive networks and resulting in a higher $\Delta R/R_0$ value.

During the subsequent retraction cycle process, the decrease of the distance between the adjacent RGO particles and the reconstruction of conductive networks lead to a decrease in the $\Delta R/R_0$ value. However, at the end of unloading, the slippage of overlapped RGO layers caused by the hysteresis effect resulting from matrix viscoelastic effects leads to an irreversible resistance change.¹⁷ It is believed that the slippage of overlapped RGO layers is attributed to the wrinkling or crimping of RGO during the extension–retraction process.⁵¹ Moreover, due to the two-dimensional layered structure of RGO, the interconnection of RGO through plane-to-plane contact easily deteriorated under tension. Therefore, an increase of the min $\Delta R/R_0$ value is observed due to the irreversible destruction of vulnerable conductive paths. With the increase of the cycle number, the distances between adjacent RGO particles are further increased and the partially conductive network is further deteriorated, leading to a gradual increase in the max and min $\Delta R/R_0$ values. Similar phenomena can also be observed in 0.3-RGO/PLA and 0.8-RGO/PLA nanocomposites (Fig. S3, ESI†).

In contrast, the max and min $\Delta R/R_0$ values of the CNTs/PLA nanocomposites decrease gradually during 10 cycles (Fig. 8d and f). Due to the one-dimensional long flexible tube structure and entangled characteristic of CNTs, the conductive network constructed by CNTs is extremely stable. The stable conductive network is effective in resisting the damage to the conductive path during cycles. Additionally, the conductive networks constructed by CNTs might be rearranged due to the hysteresis

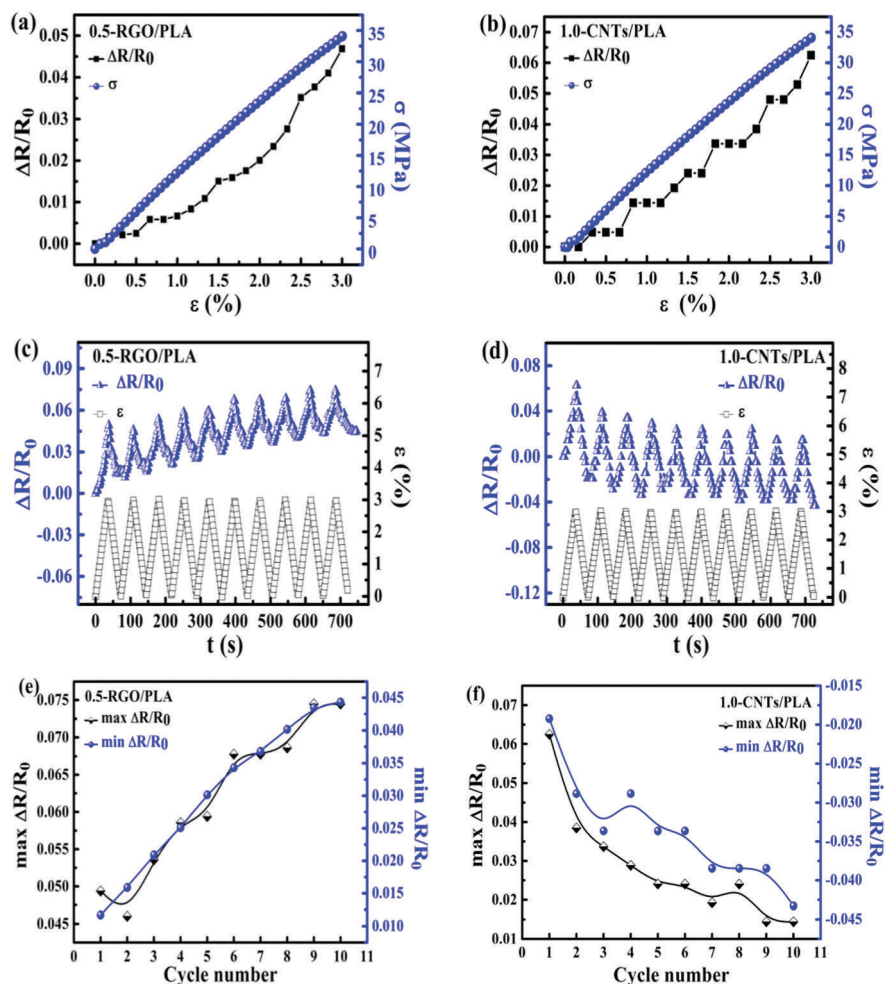


Fig. 8 $\Delta R/R_0$ (left axis) and tensile stress (right axis) plotted as a function of strain for nanocomposites during the first cycle: (a) 0.5-RGO/PLA and (b) 1.0-CNTs/PLA nanocomposites; relationships of $\Delta R/R_0$ and strain vs. time of (c) 0.5-RGO/PLA and (d) 1.0-CNTs/PLA nanocomposites during 10 extension–retraction cycles; relationship of $\max \Delta R/R_0$ and $\min \Delta R/R_0$ vs. cycle number of (e) 0.5-RGO/PLA and (f) 1.0-CNTs/PLA nanocomposites.

effect resulting from the viscoelastic behavior of CNTs/PLA on the molecular level,⁵² resulting in the formation of better conductive networks along the tensile direction. Therefore, the gradual

decrease of the max and min $\Delta R/R_0$ values is displayed. Similar phenomena can also be observed in 1.2-CNTs/PLA and 1.6-CNTs/PLA nanocomposites (Fig. S4, ESI†).

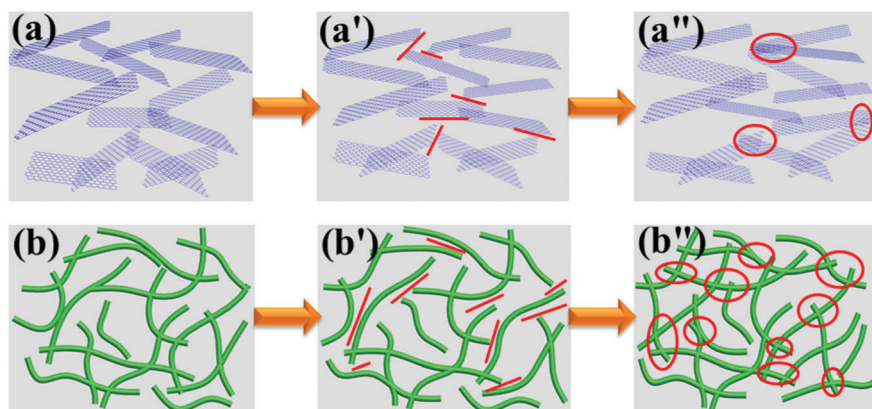


Fig. 9 Schematic illustration of the structural evolution of RGO/PLA (a–a'') and CNTs/PLA (b–b'') nanocomposites under applied dynamic loads: (a and b) initial state; (a' and b') the state in the tensile process; and (a'' and b'') the final state of filler distribution. The red lines and circles represent the damage and reconstruction of the conductive paths.

3.7. Mechanism of strain-sensing behaviors

Based on the results and discussion, the mechanism of the strain-sensing behaviors between RGO/PLA and CNTs/PLA nanocomposites is explained by a group of schematic illustrations as shown in Fig. 9. Fig. 9(a and b) show the original state of the conductive network before stretch loading. It can be seen that RGO with a two-dimensional layered structure constructs conductive networks in the matrix continuously through plane-to-plane contact; fine conductive networks of CNTs/PLA nanocomposites are also formed by the entanglement of CNTs. When the polymer matrix is deformed, the interfacial stress transfers from the polymer matrix to RGO. However, the graphene cannot match the strain of the PLA matrix and the interfacial stress fails to transfer between the two outer graphene layers,⁵³ leading to the breakdown of conductive networks constructed by graphene. During this process, due to the one-dimensional tube characteristic, the stress transfer at the CNTs–PLA interface induces the orientation of CNTs in the composites,^{8,54} and new entanglements are also formed as the CNTs collide with each other at the same time. Fig. 9(a' and b') display the state in the tensile process under an applied strain. It indicates that the breakdown of conductive networks is more prominent than the formation of new ones. For RGO/PLA nanocomposites, although some new conductive paths are formed during the retraction process, the number of interconnections between adjacent RGO decreases obviously after this cycle due to the slippage of overlapped RGO layers (Fig. 9a''), leading to an increase in max and min $\Delta R/R_0$ (Fig. 8e and Table S1, ESI[†]). For the CNTs/PLA nanocomposites, during the retraction process, the entanglement between CNTs and a large overlap length are constructed due to the one-dimensional tube characteristic. Therefore, some new conductive paths are formed and a better conductive network is preserved at the end of this cycle along the tensile direction (Fig. 9b''), leading to decreasing max and min $\Delta R/R_0$ (Fig. 8f and Table S1, ESI[†]).

4. Conclusion

PLA based CPCs containing CNTs and RGO nanofillers with different dimensions were prepared. The percolation threshold of the RGO/PLA nanocomposites (0.11 wt%) was much lower than that of the CNTs/PLA nanocomposites (0.80 wt%). Both the RGO and CNT nanofillers exhibited nanoconfinement/nucleation effects for the PLA polymer matrix during crystallization. Compared to one-dimensional CNTs, which had a stronger ability to induce the crystallization of PLA due to their strong nucleation effect, the two-dimensional RGO showed a weak ability. In addition, the thermal stability of the PLA matrix under nitrogen was different due to the incorporation of different dimensional nanofillers. RGO could enhance the thermal stability of the PLA matrix due to its strong mass barrier effect, while the thermal stability of the PLA based composite was reduced by the addition of CNTs due to its good heat conductivity but poor mass barrier effect. For the RGO/PLA nanocomposites, owing to the slippage of overlapped RGO layers, the vulnerable conductive network formed by RGO was destroyed gradually during the

extension–retraction cycles, leading to an increase in max and min $\Delta R/R_0$. However, for the CNTs/PLA nanocomposites, a better conductive network was gradually formed along the tensile direction, leading to a decrease in max and min $\Delta R/R_0$. It is evident that the distinction in the morphology and microstructure of these two fillers results in obviously different strain-sensing behaviors of the nanocomposites. An excellent strain sensor ensures a stable response to the applied strain, which is closely related to the conductive network formed by nanofillers. The investigation on the microstructure evolution of a conductive network constructed by different geometric nanofillers provides a guideline for the design and fabrication of strain sensing devices in a variety of applications, including artificial skin, soft robotics, human motion monitoring, flexible electronics, *etc.*

Acknowledgements

The authors gratefully acknowledge the financial support of this work by the National Natural Science Foundation (contract number 51603193, 11572290, 11432003), the National Natural Science Foundation of China-Henan Province Joint Funds (contract number U1604253), the China Postdoctoral Science Foundation (contract number 2015M580637, 2016T90675) and the Special Science Foundation for Excellent Youth Scholars of Zhengzhou University (contract number 1421320041). Z. Guo appreciates the start-up fund from University of Tennessee Knoxville.

References

- (a) Y. Khan, A. E. Ostfeld, C. M. Lochner, A. Pierre and A. C. Arias, *Adv. Mater.*, 2016, **28**, 4373–4395; (b) J. Gu, X. Meng, Y. Tang, Y. Li, Q. Zhuang and J. Kong, *Composites, Part A*, 2017, **92**, 27–32; (c) J. Gu, C. Liang, X. Zhao, B. Gan, H. Qiu, Y. Guo, X. Yang, Q. Zhang and D. Wang, *Compos. Sci. Technol.*, 2017, **139**, 83–89; (d) J. Gu, Z. Lv, Y. Wu, Y. Guo, L. Tian, H. Qiu, W. Li and Q. Zhang, *Composites, Part A*, 2017, **94**, 209–216.
- T. Q. Trung, S. Ramasundaram and N. E. Lee, *Adv. Funct. Mater.*, 2015, **25**, 1745–1754.
- S.-H. Hwang, D. Kang, R. S. Ruoff, H. S. Shin and Y.-B. Park, *ACS Nano*, 2014, **8**, 6739–6747.
- Y. Li, L. Hong, Y. Chen, H. Wang, X. Lu and M. Yang, *Sens. Actuators, B*, 2007, **123**, 554–559.
- B. Zhang, R. W. Fu, M. Q. Zhang, X. M. Dong, P. L. Lan and J. S. Qiu, *Sens. Actuators, B*, 2005, **109**, 323–328.
- Y. Li, H. Liu, K. Dai, G. Zheng, C. Liu, J. Chen and C. Shen, *Sens. Actuators, B*, 2015, **221**, 1279–1289.
- K. Li, K. Dai, X. Xu, G. Zheng, C. Liu, J. Chen and C. Shen, *Colloid Polym. Sci.*, 2013, **291**, 2871–2878.
- L. Lin, S. Liu, Q. Zhang, X. Li, M. Ji, H. Deng and Q. Fu, *ACS Appl. Mater. Interfaces*, 2013, **5**, 5815–5824.
- S. Zhao, J. Li, D. Cao, Y. Gao, W. Huang, G. Zhang, R. Sun and C. P. Wong, *J. Mater. Chem. C*, 2016, **4**, 6666–6674.

- 10 J. J. Park, W. J. Hyun, S. C. Mun, T. P. Yong and O. O. Park, *ACS Appl. Mater. Interfaces*, 2015, **7**, 6317–6324.
- 11 L. Vertuccio, V. Vittoria, L. Guadagno and F. De Santis, *Composites, Part A*, 2015, **71**, 9–16.
- 12 V. Eswaraiah, S. S. J. Aravind, K. Balasubramaniam and S. Ramaprabhu, *Macromol. Chem. Phys.*, 2013, **214**, 2439–2444.
- 13 R. Zhang, H. Deng, R. Valenca, J. Jin, Q. Fu, E. Bilotti and T. Peijs, *Compos. Sci. Technol.*, 2013, **74**, 1–5.
- 14 V. Eswaraiah, K. Balasubramaniam and S. Ramaprabhu, *Nanoscale*, 2012, **4**, 1258–1262.
- 15 R. Moriche, M. Sánchez, A. Jiménez-Suárez, S. Prolongo and A. Ureña, *Compos. Sci. Technol.*, 2016, **123**, 65–70.
- 16 J. R. Lu, W. G. Weng, X. F. Chen, D. J. Wu, C. L. Wu and G. H. Chen, *Adv. Funct. Mater.*, 2005, **15**, 1358–1363.
- 17 H. Liu, Y. Li, K. Dai, G. Zheng, C. Liu, C. Shen, X. Yan, J. Guo and Z. Guo, *J. Mater. Chem. C*, 2016, **4**, 157–166.
- 18 J. Zhao, K. Dai, C. Liu, G. Zheng, B. Wang, C. Liu, J. Chen and C. Shen, *Composites, Part A*, 2013, **48**, 129–136.
- 19 D. Wu, Y. Cheng, S. Feng, Z. Yao and M. Zhang, *Ind. Eng. Chem. Res.*, 2013, **52**, 6731–6739.
- 20 M. Sabzi, L. Jiang, F. Liu, I. Ghasemi and M. Atai, *J. Mater. Chem. A*, 2013, **1**, 8253–8261.
- 21 D. Zhang, B. Chi, B. Li, Z. Gao, Y. Du, J. Guo and J. Wei, *Synth. Met.*, 2016, **217**, 79–86.
- 22 Y. Fu, L. Liu and J. Zhang, *ACS Appl. Mater. Interfaces*, 2014, **6**, 14069–14075.
- 23 C. Chen, G. Lv, C. Pan, M. Song, C. Wu, D. Guo, X. Wang, B. Chen and Z. Gu, *Biomed. Mater.*, 2007, **2**, L1–L4.
- 24 J. M. Anderson and M. S. Shive, *Adv. Drug Delivery Rev.*, 2012, **64**, 72–82.
- 25 M. Amjadi, K. U. Kyung, I. Park and M. Sitti, *Adv. Funct. Mater.*, 2016, **26**, 1678–1698.
- 26 Y. S. Rim, S. H. Bae, H. Chen, M. N. De and Y. Yang, *Adv. Mater.*, 2016, **28**, 4415–4440.
- 27 T. Q. Trung and N. E. Lee, *Adv. Mater.*, 2016, **28**, 4338–4372.
- 28 J. Li, S. Zhao, X. Zeng, W. Huang, Z. Gong, G. Zhang, R. Sun and C. P. Wong, *ACS Appl. Mater. Interfaces*, 2016, **8**, 18954–18961.
- 29 J. Li, G. Zhang, R. Sun and C. Wong, *J. Mater. Chem. C*, 2016, **4**, 6666–6674.
- 30 J. Li, G. Zhang, L. Deng, S. Zhao, Y. Gao, K. Jiang, R. Sun and C. Wong, *J. Mater. Chem. A*, 2014, **2**, 20642–20649.
- 31 J. J. Park, W. J. Hyun, S. C. Mun, Y. T. Park and O. O. Park, *ACS Appl. Mater. Interfaces*, 2015, **7**, 6317–6324.
- 32 R. Zhang, Q. Chen, Z. Zhen, X. Jiang, M. Zhong and H. Zhu, *ACS Appl. Mater. Interfaces*, 2015, **7**, 19145–19152.
- 33 Kenry, J. C. Yeo, J. Yu, M. Shang, K. P. Loh and C. T. Lim, *Small*, 2016, **12**, 1593–1604.
- 34 Z. Chen, W. Ren, L. Gao, B. Liu, S. Pei and H.-M. Cheng, *Nat. Mater.*, 2011, **10**, 424–428.
- 35 D. J. Lipomi, M. Vosgueritchian, B. C. Tee, S. L. Hellstrom, J. A. Lee, C. H. Fox and Z. Bao, *Nat. Nanotechnol.*, 2011, **6**, 788–792.
- 36 J. Y. Nam, S. S. Ray and M. Okamoto, *Macromolecules*, 2003, **36**, 7126–7131.
- 37 D. Battagazzore, S. Bocchini and A. Frache, *EXPRESS Polym. Lett.*, 2011, **5**, 849–858.
- 38 J. Xu, J. Zhang, W. Gao, H. Liang, H. Wang and J. Li, *Mater. Lett.*, 2009, **63**, 658–660.
- 39 G. Wang, J. Yang, J. Park, X. Gou, B. Wang, H. Liu and J. Yao, *J. Phys. Chem. C*, 2008, **112**, 8192–8195.
- 40 Y. Cao, J. Feng and P. Wu, *Carbon*, 2010, **48**, 3834–3839.
- 41 J. N. Gavvani and H. Adelnia, *J. Mater. Sci.*, 2014, **49**, 243–254.
- 42 Z. Kulinski and E. Piorkowska, *Polymer*, 2005, **46**, 10290–10300.
- 43 C. Bao, L. Song, W. Xing, B. Yuan, C. A. Wilkie, J. Huang, Y. Guo and Y. Hu, *J. Mater. Chem.*, 2012, **22**, 6088–6096.
- 44 R. Socher, B. Krause, R. Boldt, S. Hermasch, R. Wursche and P. Pötschke, *Compos. Sci. Technol.*, 2011, **71**, 306–314.
- 45 X.-Y. Qi, D. Yan, Z. Jiang, Y.-K. Cao, Z.-Z. Yu, F. Yavari and N. Koratkar, *ACS Appl. Mater. Interfaces*, 2011, **3**, 3130–3133.
- 46 X. Hu, E. Su, B. Zhu, J. Jia, P. Yao, Y. Bai, X. Hu, E. Su, B. Zhu and J. Jia, *Compos. Sci. Technol.*, 2014, **97**, 6–11.
- 47 M. M. Rahman, S. Zainuddin, M. V. Hosur, J. E. Malone, M. Salam, A. Kumar and S. Jeelani, *Compos. Struct.*, 2012, **94**, 2397–2406.
- 48 J. J. Ku-Herrera and F. Avilés, *Carbon*, 2012, **50**, 2592–2598.
- 49 J. Du, L. Zhao, Y. Zeng, L. Zhang, F. Li, P. Liu and C. Liu, *Carbon*, 2011, **49**, 1094–1100.
- 50 Z. H. Ni, T. Yu, Y. H. Lu, Y. Y. Wang, Y. P. Feng and Z. X. Shen, *ACS Nano*, 2008, **2**, 2301–2305.
- 51 Q. C. Tan, R. A. Shanks and D. Hui, *Composites, Part B*, 2016, **90**, 315–325.
- 52 M. H. G. Wichmann, S. T. Buschhorn, J. Gehrman and K. Schulte, *Phys. Rev. B: Condens. Matter Mater. Phys.*, 2009, **80**, 245437.
- 53 T. Jiang, R. Huang and Y. Zhu, *Adv. Funct. Mater.*, 2014, **24**, 396–402.
- 54 M. Mu, S. Osswald, Y. Gogotsi and K. I. Winey, *Nanotechnology*, 2009, **20**, 335703.